Materials and Manufacturing Processes, 24: 384–397, 2009

ISSN: 1042-6914 print/1532-2475 online
DOI: 10.1080/10426910802679915

A Genetic Algorithm-Assisted Inverse Convective Heat Transfer Model for Tailoring Weld Geometry

S. Bag[1], A. De[1], and T. DebRoy[2]

[1]*Mechanical Engineering Department, IIT Bombay, Mumbai, India*
[2]*Materials Science and Engineering Department, The Pennsylvania State University, Pennsylvania, USA*

Although heat transfer and fluid flow models have provided significant insight about the welding processes and welded materials, currently they are not widely used, mainly because of two difficulties. First, the model predictions do not always agree with experiments because the values of energy absorption efficiency and other parameters cannot be prescribed from scientific principles. Second, the available models are unidirectional and cannot currently predict welding variables necessary to attain a target weld attribute. Here we provide a rigorous proof that the heat transfer and fluid flow models can be combined with an appropriate genetic algorithm (GA) to enhance reliability of computational results and achieve inverse modeling capability. The new capability enables systematic tailoring of weld attributes based on scientific principles. In particular, the GA-based optimization of arc efficiency, arc radius, effective thermal conductivity, and effective viscosity using a limited volume of experimental data led to superior weld geometry computations for a wide variety of welding conditions. Furthermore, the inverse model's ability to calculate multiple combinations of arc current, voltage, and welding speed needed to achieve a target weld geometry was developed and rigorously tested by welding experiments.

Keywords Arc welding; Convective heat transfer; Genetic algorithm; Inverse model; Numerical optimization.

1. Introduction

Numerical modeling of heat transfer and fluid flow is often used for the estimation of temperature fields and fusion zone geometry in various welding processes [1–4]. Furthermore, the computed thermal cycles have been used to understand weld metal phase composition [5, 6], grain structure [7], and weld metal composition changes [8]. However, the numerical heat transfer and fluid flow models for welding have so far been used mostly as a research tool [9, 10], rather than as a tool for designing and manufacturing in the industry.

There are several reasons for the restricted use of heat transfer and fluid flow modeling in welding at this time. First, the current numerical models for these calculations in welding require several input parameters that cannot be accurately specified based on scientific principles. For example, the value of arc efficiency varies significantly with the nature of the material, and the value of the arc radius depends on welding conditions. Values of the effective thermal conductivity and effective viscosity are used to accurately model transport of heat and momentum in the weld pool. They are properties of the specific welding system and not inherent physical properties of the liquid metal [11–16]. The uncertainty in the values of these parameters affects the quality of the computed results and jeopardizes close agreement between the experimental and the computed results. In fact, all phenomenological computational models of fusion welding now lack a structural component to achieve closure with experimental data. Disagreements between the experimental and the modeling results are a powerful disincentive for the widespread use of the computational models. Second, the available heat transfer and fluid flow models of welding are unidirectional and cannot currently predict welding variables to attain a target weld attribute. Therefore, they cannot now be used to tailor weld attributes. Systematic tailoring of weld attributes based on scientific principles still remains an important goal in fabricating reliable welds. Such tailoring requires inverse modeling capability and can prevent catastrophic failures of large structures, save life and property, and is important for both the infrastructure and our contemporary standard of living.

Here we show that when the convective heat transfer model is integrated with a genetic algorithm (GA), the optimum values of the arc efficiency, effective arc radius, effective thermal conductivity, and effective viscosity can be determined from a set of known weld dimensions. Similar efforts by linking classical gradient-based search techniques with numerical heat transfer and fluid flow model to identify suitable values of uncertain input parameters have been reported in the recent past [12–15]. However, the gradient-based search techniques are not optimum in the sense that they can be trapped in local minima and require the objective function and its derivatives to be continuous within the search space. In contrast, stochastic optimization techniques, such as the genetic algorithms [17–22] can overcome these difficulties and are capable of finding the global solution. Here we show that a convective heat transfer model when combined with a global search technique such as GA can identify global optimum values of uncertain model input variables.

We further show that an integrated heat transfer and fluid flow model combined with a GA-based optimization scheme can be used as an inverse model to find various

Received July 24, 2008; Accepted November 30, 2008

Address correspondence to T. DebRoy, Materials Science and Engineering Department, The Pennsylvania State University, University Park, PA 16802, USA; E-mail: debroy@psu.edu

combinations of welding variables needed to achieve a target weld pool geometry. A desired weld attribute such as geometry can be produced using multiple welding variable sets. The inverse model can be used to calculate alternative combinations of welding variables to achieve a target weld geometry. The effectiveness of the approach is checked by conducting experiments using the computed welding variables and comparing the geometry produced in each case with the target weld geometry.

A large body of existing literature involving synthesis of fluid flow calculations with generic algorithms for the solution of several problems indicates that the approach adapted in this article is promising. The reader is refereed to Ref. [20] for a review of how GA can be utilized in materials design and processing, and Refs. [12–15] and [23–25] as examples of how GA can be combined with fluid flow to solve important problems. Both the genetic algorithms as well as the numerical heat transfer and fluid flow calculations are computationally intensive. Only because of recent advances in computational hardware and software, the tasks of improving reliability of calculations and GA-assisted tailoring weld attributes based on scientific principles can now be undertaken.

2. Heat transfer and fluid flow simulation

The flow of incompressible Newtonian liquid metal in the weld pool is computed assuming a flat weld pool surface because the weld pool depression is small for the welding currents used in this study. The density variation with temperature is ignored because it is small, except for the calculation of the buoyancy force following Boussinesq's approximation. The weld cross-section does not change with time except at the beginning and the end of welding and a quasi-steady state assumption is appropriate except for the two ends of the welds. A Cartesian co-ordinate system where the heat source moves at a constant welding speed, U, in the negative x-direction, is adapted. In the moving co-ordinate system, the system of momentum conservation equations can be written as [26]

$$\rho\frac{\partial(u_i u_j)}{\partial x_i} = \frac{\partial}{\partial x_i}\left(\mu\frac{\partial u_j}{\partial x_i}\right) - \rho U\frac{\partial u_j}{\partial x_1} - \frac{\partial p}{\partial x_j} + \rho g_j\beta(T - T_r) + S_j. \tag{1}$$

In the above equation, ρ is the density, x_i is the distance along the $i = 1, 2$, and 3 (same as x, y, and z) orthogonal directions, u is the velocity in the direction shown by its subscript, μ is the effective viscosity, p is modified pressure obtained by subtracting hydrostatic pressure from local pressure, g_j is the acceleration due to gravity which is zero except in the vertical direction (direction 3 or z), β is the coefficient of volume expansion, T is temperature, T_r is the reference temperature, and S_j is the source term given as

$$S_j = -c_m\left(\frac{(1 - f_L)^2}{f_L^3 + b}\right)u_j + (J \times B)_j + \frac{\partial}{\partial x_i}\left(\mu\frac{\partial u_i}{\partial x_j}\right), \tag{2}$$

where f_L is the liquid fraction, c_m (1.6×10^4 kg/(m^{3}s)) is a constant that takes into account mushy zone morphology and b is a constant introduced to avoid division by zero. The first term on the right-hand side (RHS) represents the frictional dissipation in the mushy zone according to the Carman–Kozeny equation for flow through a porous media [27, 28]. The second term represents the electromagnetic force field and the calculation of the electromagnetic force field is discussed in Appendix B. More details are available in a recent article [29]. The value of the effective viscosity in Eq. (1) is a property of the specific welding system and not an inherent property of the liquid metal. Typical values of effective viscosity are much higher than that of the molecular viscosity [30]. The higher value is important, since it allows accurate modeling of the high rates of transport of momentum in systems with strong fluctuating velocities that are inevitable in small weld pools with very strong convection currents. The pressure field was obtained by solving the following continuity equation simultaneously with the momentum equation:

$$\frac{\partial(\rho u_i)}{\partial x_i} = 0. \tag{3}$$

The total enthalpy H is represented by a sum of sensible heat h and latent heat content ΔH, i.e., $H = h + \Delta H$, where $h = \int C_p dT$, C_p is the specific heat, $\Delta H = f_L L$, L is the latent heat of fusion, and the liquid fraction f_L is assumed to vary linearly with temperature in the mushy zone:

$$f_L = \begin{cases} 1 & T > T_L \\ \dfrac{T - T_S}{T_L - T_S} & T_S \le T \le T_L \\ 0 & T < T_S \end{cases}, \tag{4}$$

where T_L and T_S are the liquidus and solidus temperature, respectively. The steady state transport of heat in the weld workpiece can be expressed by the following modified energy equation:

$$\rho\frac{\partial(u_i h)}{\partial x_i} = \frac{\partial}{\partial x_i}\left(\frac{k}{C_p}\frac{\partial h}{\partial x_i}\right) - \rho\frac{\partial(u_i\Delta H)}{\partial x_i} - \rho U\frac{\partial h}{\partial x_1} - \rho U\frac{\partial(\Delta H)}{\partial x_1}, \tag{5}$$

where k is the thermal conductivity. In the liquid region, the value of the thermal conductivity in Eq. (5) is taken as the effective thermal conductivity which is a property of the specific welding system and not an inherent property of the liquid metal. Typical values of effective thermal conductivity are much higher than that of the thermal conductivity of the liquid. The higher value is important, since it allows accurate modeling of the high rates of transport of heat in systems with strong fluctuating velocities that are inevitable in small weld pools with very strong convection currents. Since the weld is symmetrical about the weld center line only half of the workpiece

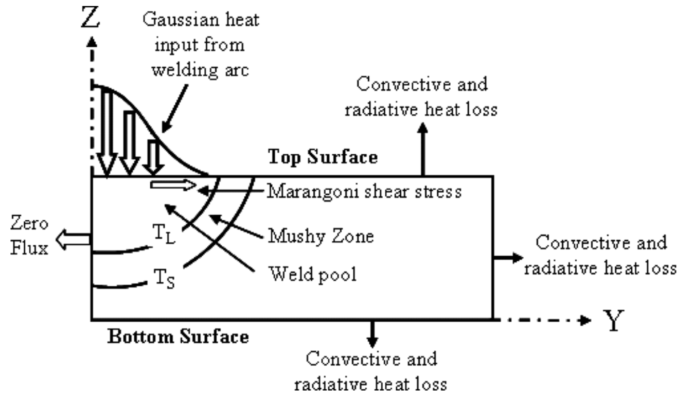

FIGURE 1.—A cross-section of the weld showing boundary conditions.

is considered. Figure 1 schematically shows the solution domain along with the applied boundary conditions. By balancing tangential (viscous) stresses and surface tension on the assumed flat surface of the melt, the velocity boundary conditions for the horizontal components of velocity are given by Eqs. (6a) and (6b). Furthermore, since there is no normal velocity on the weld pool surface, the vertical component of velocity, w is zero as indicated in Eq. (6c):

$$\mu \frac{\partial u}{\partial z} = f_L \frac{d\gamma}{dT} \frac{\partial T}{\partial x} \tag{6a}$$

$$\mu \frac{\partial v}{\partial z} = f_L \frac{d\gamma}{dT} \frac{\partial T}{\partial y} \tag{6b}$$

$$w = 0 \tag{6c}$$

where u, v, and w are the velocity components along the x, y, and z directions, respectively, and $d\gamma/dT$ is the temperature coefficient of surface tension. As shown in Eq. (6), the u and v velocities are determined from the Marangoni effect. The w velocity is equal to zero since there is no flow of liquid metal perpendicular to the pool top surface. The heat flux at the top surface is given as

$$k\frac{\partial T}{\partial z} = \frac{dQ\eta}{\pi r_b^2} \exp\left(-\frac{d(x^2+y^2)}{r_b^2}\right) - \sigma\varepsilon\left(T^4 - T_a^4\right) - h_c(T - T_a), \tag{7}$$

where r_b is the arc radius, d is the arc power distribution factor, Q is the total arc power, η is the arc efficiency, σ is the Stefan–Boltzmann constant, h_c is the heat transfer coefficient, and T_a is the ambient temperature. The first term on the right-hand side is the heat input from the heat source, defined by a Gaussian heat distribution. The second and third terms represent the heat loss by radiation and convection, respectively. The boundary conditions are defined as zero flux across the symmetric surface (i.e., at $y = 0$) as

$$\frac{\partial u}{\partial y} = 0 \tag{8a}$$

$$v = 0 \tag{8b}$$

$$\frac{\partial w}{\partial y} = 0 \tag{8c}$$

$$\frac{\partial h}{\partial y} = 0. \tag{9}$$

At all other surfaces, temperatures are set at ambient temperature, and all velocities are set to zero.

The governing equations are discretized using the control volume method in the following form [26]

$$a_P\phi_P = \sum_{nb}(a_{nb}\phi_{nb}) + S_U\Delta V, \tag{10}$$

where subscript P represents a given grid point, while subscript nb represents the neighbors of the given grid point P, ϕ is a general variable such as velocity or enthalpy, a is the coefficient calculated based on the power law scheme, and ΔV is the control volume. The coefficient a_P is defined as

$$a_P = \sum_{nb} a_{nb} - S_P\Delta V. \tag{11}$$

The terms S_U and S_P are used in the source term linearization as

$$S = S_U + S_P\phi_P \tag{12}$$

and solved by a Gaussian elimination technique known as tridiagonal matrix algorithm (TDMA) [26]. Scalar grid points are located at the center of each control volume, whereas the velocity components are staggered with respect to scalar locations to achieve improved stability and convergence of numerical calculations. The discretized equations are solved using SIMPLE algorithm [26] using constant thermophysical properties to make the calculations tractable.

Two convergence criteria are used, i.e., residuals and heat balance. The residuals for velocities and enthalpy are defined as

$$R = \frac{\sum_{\text{domain}} \left| \frac{\sum_{nb}(a_{nb}\phi_{nb}) + S_U\Delta V}{a_P} - \phi_P \right|}{\sum_{\text{domain}} |\phi_P|}. \tag{13}$$

The residual values should be usually very small (typically 10^{-4}) when a converged solution is obtained. The following overall heat balance check provides another criterion for the convergence of the solution:

$$\theta = \left| \frac{\text{net heat input}}{\text{total heat out}} \right|. \tag{14}$$

Convergence is assumed when $R \le 10^{-4}$ and $0.99 \le \theta \le 1.01$. More strict convergence criteria do not change the final results but increase computational time.

3. A GA-assisted optimization procedure

GA is utilized for two specific tasks here. First, it is used for determining the values of four uncertain input parameters, arc efficiency, arc radius, effective thermal conductivity, and effective viscosity that are inputs to the heat transfer and fluid flow model. These parameters cannot be specified based on fundamental principles, and yet their values affect the computed temperature and velocity fields from which the weld geometry is calculated. For this purpose, a GA is used to determine the optimum values of these parameters by using the forward convective heat transfer model and a set of four experimentally determined weld geometries for four welding conditions (marked by $*$ in Table 1). Because the procedure involves closure with the experimental data, the calculations of the optimized values of the parameters lead to better predictions from the forward convective heat transfer model. Second, a GA-based optimization scheme can be used with the forward heat transfer and fluid flow model to achieve an inverse modeling capability, i.e., to find various combinations of welding variables needed to achieve a target weld pool geometry.

A parent-centric recombination (PCX)-based generalized generation gap (G3) real number GA was used to obtain the optimized values of the four unknown variables indicated before. A suitable objective function, which is sensitive to the unknown variables, is required for the calculations. The PCX G3 model uses probability distributions of the selected old individuals (parents) for the generation of new individuals (offspring) and the subsequent selection of the most potential offspring in an iterative manner. This GA is selected for its fast convergence rate and its ability to provide multiple solutions where such solutions are meaningful [18, 19].

The objective function, $O(f)$, is defined as the sum of the squared error between the computed and the corresponding measured values of weld width and penetration as

$$O(f) = \sum_{m=1}^{M} \left\{ \left(\frac{w_m^c - w_m^{obs}}{w_m^{obs}} \right)^2 + \left(\frac{p_m^c - p_m^{obs}}{p_m^{obs}} \right)^2 \right\} = \sum_{m=1}^{M} \left\{ (w_m^* - 1)^2 + (p_m^* - 1)^2 \right\}, \tag{15}$$

where p_m^c, w_m^c, p_m^{obs}, and w_m^{obs} refer, respectively, to the computed values of weld penetration and width, and their corresponding measured values for mth welding condition. The terms p_m^* and w_m^* are nondimensional and indicate the extent of over or under-prediction of weld penetration and width, respectively. The subscript m refers to a specific welding condition in a series of M number of total welds. In the first set of optimization calculations, the term, f, in Eq. (15) refers to a set of four given unknown parameters as

$$\{f\} \equiv \{f_1 \quad f_2 \quad f_3 \quad f_4\} \equiv \{\eta \quad r^* \quad k^* \quad \mu^*\} \equiv \left\{ \eta \quad \frac{r_b}{e_r} \quad \frac{k_{eff}}{k_S} \quad \frac{\mu}{\mu_{fl}} \right\}. \tag{16}$$

In Eq. (16), e_r, k_S, μ_{fl}, k_{eff} and μ, respectively, refer to electrode radius (~1.0 mm), thermal conductivity of solid material at room temperature, viscosity of molten iron at 1823 K, effective thermal conductivity and effective viscosity of liquid metal. All unknown parameters included in f are dimensionless. The data used in the calculations are given in Table 2. In the second optimization calculations, the term, f, in Eq. (15) refers to a set of three unknown process variables that can yield a target weld dimension as

$$\{f\} \equiv \{f_1 \quad f_2 \quad f_3\} = \left\{ \frac{I}{I_{mn}} \quad \frac{V}{V_{mn}} \quad \frac{v}{v_{mx}} \right\} = \{I^* \quad V^* \quad v^*\}, \tag{17}$$

where I and I_{mn} refer, respectively, to the target welding current and the minimum value of current in a prescribed range. Similarly, V and V_{mn}, and v and v_{mx} refer to the target welding voltage and the minimum value of voltage, and target weld velocity and the maximum value for weld velocity, respectively.

The optimization process starts with an initial population containing a number of individuals generated randomly considering the specified range of each of the variables, which are being optimized. Next, the values of $O(f)$ are computed for all the M observations corresponding to each individual that evidently requires a number of numerical heat transfer and fluid flow calculations. The best individual is decided by the fitness value that is equivalent to the minimum value of $O(f)$. Next, a second population set of three individuals is created consisting of the best individual and two more from the initial population set. The second population set yields two offspring using the PCX operator. A third subsequent population set is created next consisting of the two offspring and two individuals selected randomly from the initial population set. These four individuals in the third population are ranked based on the increasing order of their corresponding values of $O(f)$. The first two individuals in the rank replace two individuals in the second population set and also in the initial population set in a random manner, thereby enriching the later with good individuals. The procedure explained above is repeated till the convergence criteria, i.e., a single or a multiple set of individuals are achieved with corresponding value(s) of $O(f)$ that is (are) lesser than the specified minimum acceptable value of $O(f)$. After the first iteration, the values of $O(f)$ are calculated only for the two new individuals generated from the second population set. A further detailed description of the PCX G3 GA optimization algorithm and the mathematical expressions are discussed in the Appendix A.

4. Experiments

A set of eight autogenous welds were made in 3.0 mm thick austenitic stainless steel (SS304) plates using an AC/DC gas tungsten arc (GTA) welding power source in direct current electrode negative (DCEN) polarity. A 2% thoriated tungsten electrode of 2 mm diameter and 45° tip angle is used for all the welds. The electrode is positioned normal to the work piece with a constant arc length of 3 mm. Table 1 shows

TABLE 1.—Welding variables and experimentally measured weld pool dimensions.

Data set index	Current (A)	Voltage (V)	Weld velocity (mm/s)	Weld width (mm)	Weld penetration (mm)
*1	120	11.6	5.0	4.51	1.24
*2	140	11.0	5.0	4.71	1.36
3	180	12.0	5.0	6.10	1.91
*4	140	11.2	7.0	4.47	1.23
5	180	12.6	7.0	4.81	1.63
*6	200	13.8	7.0	6.11	1.83
7	180	12.3	9.0	4.78	1.36
8	200	14.3	9.0	5.42	1.62

the weld pool dimensions and the corresponding welding conditions for all the eight sample welds. The values of welding current, voltage, and the welding speed for the eight sample welds are chosen based on a set of trial-and-error experiments with a target to have sufficient weld penetration in each case without any burn-through.

5. Results and discussion

Figures 2 and 3 depict the sensitivity of the computed weld pool dimensions on the four uncertain parameters in nondimensional form, e.g., arc efficiency (η), arc radius (r^*), effective thermal conductivity (k^*), and effective viscosity (μ^*). The computed weld pool width and penetration are represented in nondimensional form as w_m^* and p_m^*, respectively. Thus, a value of one for both w_m^* and p_m^* indicates good agreement between the computed and the measured weld dimensions while values higher or lower than one indicate higher or lower than the experimental value, respectively. Figures 2(a) and (b) show the effect of η on w_m^* and p_m^* for all eight welding conditions shown in Table 1. As the value of η increases, the values of both w_m^* and p_m^* increase because of higher heat input as shown in the figures. A comparison between Figs. 2(a) and (b) indicates that w_m^* increases at a faster rate than p_m^* with η. More heat is readily distributed by Marangoni convection on the weld pool surface and the weld width increases. Figures 2(a) and (b) also indicate that values of w_m^* tend to be one at $\eta \sim 0.50$ for several welding conditions while values of p_m^* tend to be one over a wide range of η ($0.50 \sim 0.80$) for several other welding conditions.

Figures 2(c) and (d) show the influence of r^* on w_m^* and p_m^*. It is observed that with increase in r^*, the value of w_m^* increases slightly while that of p_m^* decreases. An increase in r^* indicates an increase in the arc radius and a decrease in

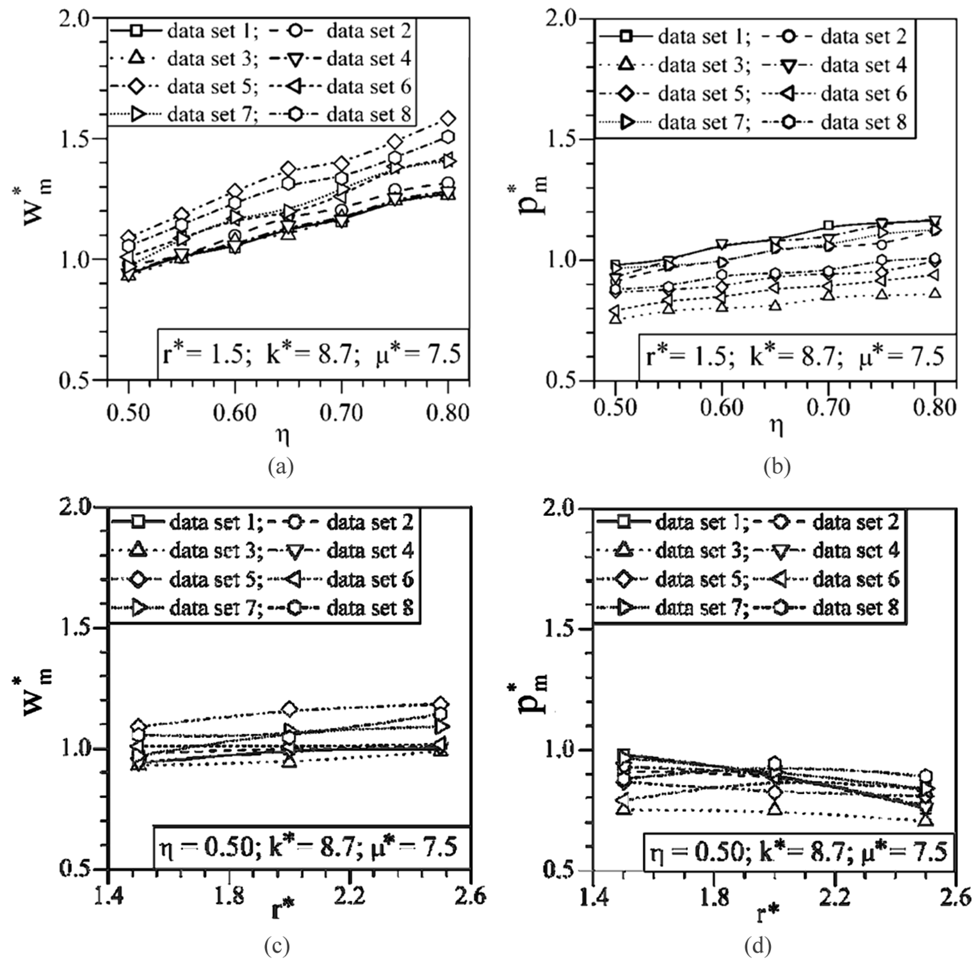

FIGURE 2.—Sensitivity of the computed values of (a) w_m^* on η; (b) p_m^* on η; (c) w_m^* on r^*; and (d) p_m^* on r^* for all eight welding conditions in Table 1.

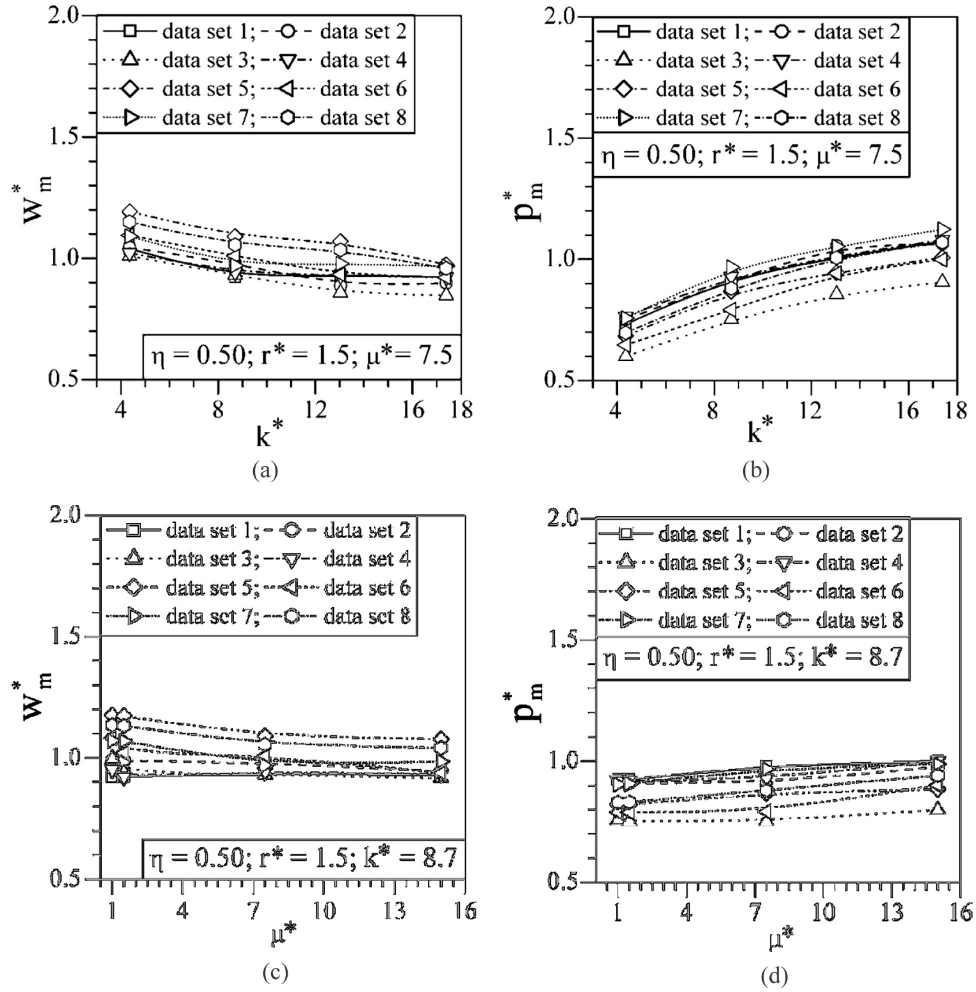

FIGURE 3.—Sensitivity of the computed values of (a) w^*_m on k^*; (b) p^*_m on k^*; (c) w^*_m on μ^*; and (d) p^*_m on μ^* for all eight welding conditions in Table 1.

power density. Thus, for a given input power, an increase in r^* leads to somewhat higher values of w^*_m and smaller values of p^*_m, since the reduced arc power density decreases the peak temperature and heat transport in the thickness direction. Nevertheless, Figs. 2(c) and (d) indicate that both w^*_m and p^*_m tend to improve when r^* is close to 1.5.

Figure 3 shows the effects of effective thermal conductivity and effective viscosity on the computed weld dimensions. Figures 3(a) and (b) show that an increase in the value of k^* reduces w^*_m and increases p^*_m. High values of k^* reduce the spatial gradient of temperature and tend to equalize the rate of conduction heat transfer in all directions. The work piece is smaller in the thickness than the other two dimensions. Thus, with the increase in k^*, the effective rate of conduction heat transfer is enhanced in the thickness direction yielding greater computed values of p^*_m. However, higher values of k^* reduce the surface temperature gradient and w^*_m. Figures 3(c) and (d) depict a similar influence of μ^* on computed values of w^*_m and p^*_m. An increase in μ^* reduces velocities, impedes convective transport of heat along the free surface of the weld pool and reduces w^*_m. The computed peak temperature is increased which increases heat transport in the depth direction and p^*_m.

Figures 3(c) and (d) also show that the computed weld pool dimensions become somewhat insensitive at higher values of μ^*. Furthermore, Figs. 3(a)–(d) show that the computed weld pool dimensions are more sensitive to the values of effective thermal conductivity than the values of effective viscosity.

Figures 2 and 3 indicate that optimization of the values of the four uncertain parameters for the eight welding conditions in Table 1 cannot be achieved graphically. Therefore, a GA-based global optimization scheme is used here. The optimization starts with randomly generated initial population and each individual consists of four values of uncertain parameters, e.g., η, r^*, k^*, and μ^* within a specified range of each of these parameters. Table 3 presents these ranges, which are primarily decided from the values of these parameters reported in the literature for similar welding process [12, 13, 31–33]. Only four welding conditions and the corresponding weld dimensions, indicated by * in Table 1 are used for the optimization of the four uncertain parameters.

Figure 4 shows the distribution of the initially generated random populations of one hundred sets of four uncertain parameters (η, r^*, k^*, and μ^*) used in the calculations.

TABLE 2.—Physical properties of SS304 used in the calculation.

Parameters	Units	Value
Density of liquid metal	$kg\,m^{-3}$	7.2×10^3
Molecular viscosity	$kg\,m^{-1}\,s^{-1}$	6.7×10^{-3}
Solidus temperature	K	1697
Liquidus temperature	K	1727
Specific heat of solid	$J\,kg^{-1}\,K^{-1}$	711.8
Specific heat of liquid	$J\,kg^{-1}\,K^{-1}$	837.4
Enthalpy of solid at melting point	$J\,kg^{-1}$	1.20×10^6
Enthalpy of liquid at melting point	$J\,kg^{-1}$	1.26×10^6
Thermal conductivity of solid	$J\,m^{-1}\,s^{-1}\,K^{-1}$	19.26
Temperature coefficient of surface tension	$N\,m^{-1}\,K^{-1}$	-0.43×10^{-3}
Magnetic permeability	$N\,A^{-2}$	1.26×10^{-6}
Coefficient of thermal expansion	K^{-1}	1.96×10^{-5}

TABLE 3.—Range of unknown parameters and their optimized value.

Uncertain parameters	Range	Optimum value
η	0.5–0.8	0.53
r^*	1.5–2.5	1.95
k^*	1.0–15.0	12.74
μ^*	1.0–15.0	10.22

Figure 5(a) shows the distribution of the computed values of objective function, $O(f)$, for the initial populations as a function of arc characteristics, i.e., η and r^*. The multiple peaks in Fig. 5(a) for different sets of values of variables indicate that multiple solutions may exist, since low values of the objective function indicate potential solutions. Figure 5(a) further demonstrates that a combination of either low values of r^* ($1.5 \sim 2.0$) and η ($0.50 \sim 0.56$) or high values of r^* ($2.0 \sim 2.4$) and η ($0.57 \sim 0.65$) tend to yield low values of $O(f)$. Figure 5(b) describes the distribution of computed values of $O(f)$ for the initial population as a function of weld pool material properties, e.g., k^* and μ^*. Figure 5(b) shows that the computed values of $O(f)$ are low for high values of k^* ($7.0 \sim 14.0$) and μ^* ($9.0 \sim 15.0$).

Figures 6(a) and (b) show the progress in the computed values of $O(f)$ after ten iterations (generations). It is observed that considerable improvement of $O(f)$ occurred for r^*, η, k^*, and μ^* in the ranges of $1.5 \sim 2.0$, $0.50 \sim 0.60$, $10.0 \sim 14.0$, and $10.0 \sim 14.0$, respectively. The corresponding values of $O(f)$ as a function of k^* and

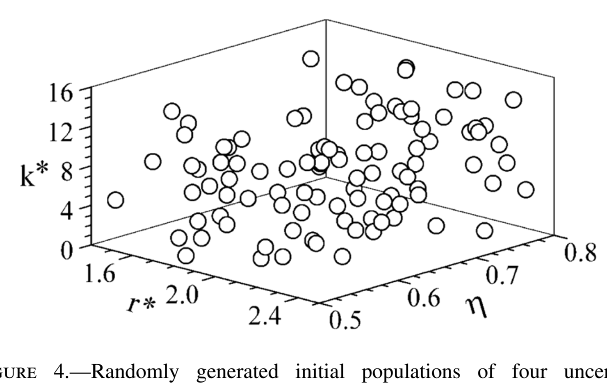

FIGURE 4.—Randomly generated initial populations of four uncertain parameters within the specified ranges shown in Table 3.

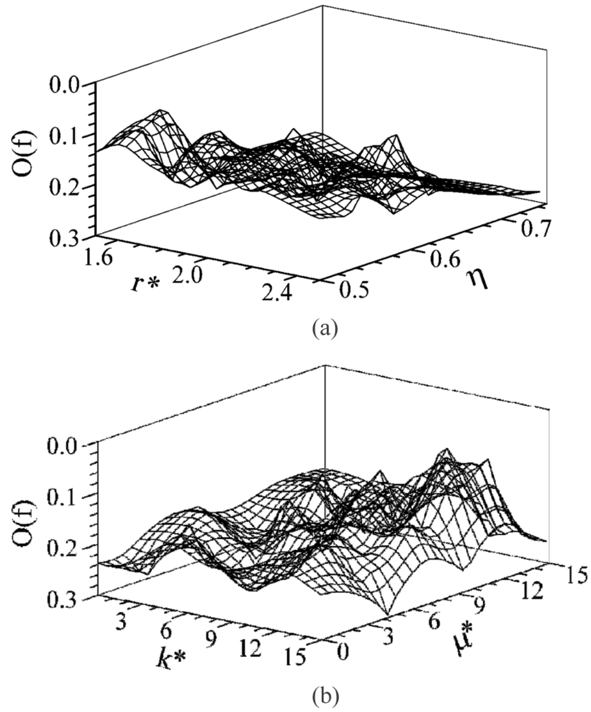

FIGURE 5.—(a) Distribution of $O(f)$ as a function of η and r^* corresponding to the initial population; (b) Distribution of $O(f)$ as a function of k^* and μ^* corresponding to the initial population.

μ^* after tenth generation are also shown in Fig. 6(b). Figures 6(c) and (d) show that a global optimum solution seems to have been achieved after the thirteenth generation with $O(f) = 4.9 \times 10^{-4}$ since more iterations did not reduce the objective function. The values of η, r^*, k^*, and μ^* are 0.53, 1.95, 12.74, and 10.22, respectively, for the minimum value of $O(f)$. Typical values of arc efficiency in GTA welding process have been reported in the range of 0.35 to 0.86 in the literature [34], and the optimum value of η is within this range. The optimum value of 1.95 mm corresponding to arc radius is justifiable for a tungsten electrode of 2.0 mm diameter and 45° tip angle. Considering the 3.0 mm arc length for all the experiments, and 60° incident angle of the arc normal to the work piece [34] the effective arc radius is approximately calculated as 1.98 mm which agrees well with the estimated optimum value (~1.95 mm). The optimum values of effective thermal conductivity and viscosity are $245.4\,W m^{-1} K^{-1}$ and $0.07\,kg\,m^{-1}\,s^{-1}$, respectively. An enhancement of 5 to 20 times in the values of effective thermal conductivity and viscosity over their corresponding molecular values are generally used to realistically account for the convective heat transport in small weld pools [9, 12–15, 35, 36]. In addition, the effective thermal conductivity and effective viscosity were found to be in the ranges of $167.5 \sim 504\,W m^{-1} K^{-1}$ and 0.06 to 0.14 Pa.s, respectively, for autogenous laser welding [35, 36]. The optimized values of the effective thermal conductivity and viscosity obtained in this work using GA are within these ranges.

Figure 7 shows a comparison of the computed weld dimensions using the optimum set of uncertain parameters

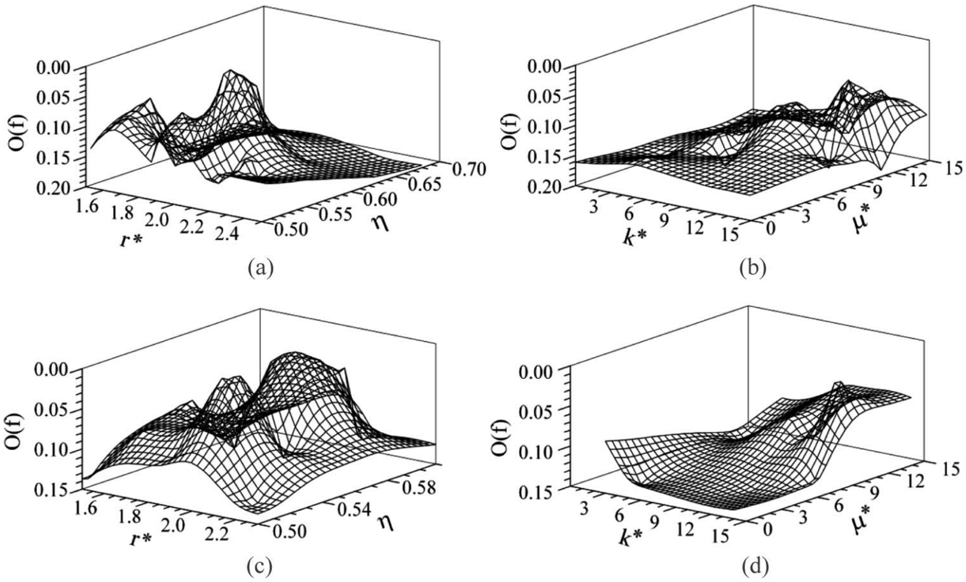

FIGURE 6.—Progress of $O(f)$ with generations as a function of uncertain parameters: (a) distribution of $O(f)$ as a function of η and r^* after tenth generation; (b) distribution of $O(f)$ as a function of k^* and μ^* after tenth generation; (c) distribution of $O(f)$ as a function of η and r^* after thirteenth generation; and (d) distribution of $O(f)$ as a function of k^* and μ^* after thirteen generation.

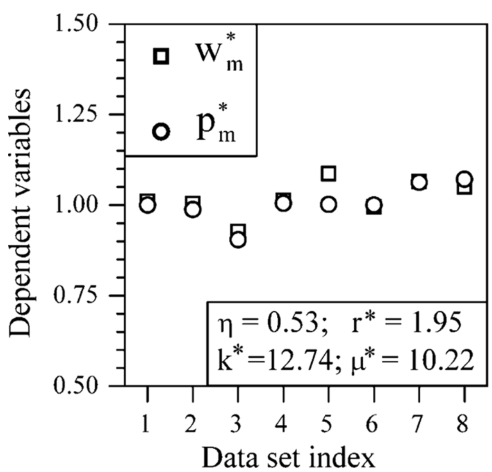

FIGURE 7.—Comparison of experimentally measured and the corresponding calculated weld pool dimensions computed using optimum set of uncertain parameters.

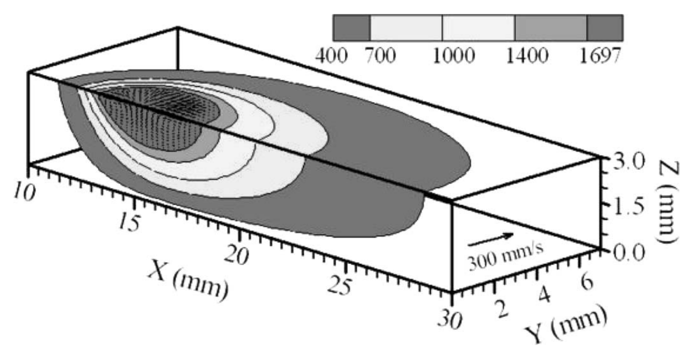

FIGURE 8.—Computed temperature (in K) and velocity fields corresponding to the welding conditions of data set index 1 in Table 1 calculated using optimum set of uncertain parameters presented in Table 3.

with the corresponding experimentally measured values for all eight data sets in Table 1. Out of the eight data sets, four were not used for optimization calculations. A fair agreement between the computed and the measured weld dimensions for all the eight data sets indicate the effectiveness of the GA-based optimization scheme. Figure 8 shows the computed temperature and velocity fields for the data set 1 in Table 1. The convective motion of liquid metal in the weld pool is mainly driven by the surface tension and electromagnetic forces and, to a much lesser extent, the buoyancy force. Since the temperature coefficient of surface tension has a negative value, the surface tension force drives the liquid metal from the middle of the weld pool to its periphery at the top surface. The maximum magnitude of velocity was approximately 115 mm/s. In the weld pool, the relative importance of heat transport by convection and conduction can be estimated from the Peclet number:

$$Pe = \frac{\rho u C_p L_C}{k_{eff}}, \tag{18}$$

where u is the maximum velocity along the top surface of weld pool, ρ the density, C_p the specific heat, k_{eff} the effective thermal conductivity of the liquid metal, and L_C is the characteristic length. The computed values of Peclet number corresponding to the eight data sets in Table 1 are shown in Table 4. The computed Peclet numbers were much higher than one for all the eight welding conditions indicating the importance of convective heat transfer within the weld pool. In Fig. 8, the region encompassed by the 1697 K isotherm confirms to final weld pool shape and

TABLE 4.—Computed values of Peclet number and non-dimensional heat input.

Data set index	Current (A)	Voltage (V)	Velocity (mm/s)	Computed Peclet no.	N_{HI}
1	120	11.6	5.0	6.3	1.39
2	140	11.0	5.0	8.2	1.53
3	180	12.0	5.0	17.1	2.15
4	140	11.2	7.0	7.2	1.11
5	180	12.6	7.0	16.2	1.61
6	200	13.8	7.0	23.9	1.96
7	180	12.3	9.0	14.4	1.22
8	200	14.3	9.0	22.7	1.58

size, and its intercepts along x, y, and z axes represent the weld length, width, and penetration, respectively. Figure 9 shows the transverse cross-section of the computed weld dimensions (on the right) and the actual weld macrographs (on the left) for four welding conditions. Good agreement between the measured and the corresponding computed weld pool shapes is achieved in all cases.

In order to compare welds for a wide range of welding conditions, a nondimensional heat input index (N_{HI}) is defined as [12, 13]

$$N_{HI} = \frac{\frac{Q\eta}{\pi r_{eff}^2 U}}{\rho C_P (T_L - T_a) + \rho L}, \tag{19}$$

where Q is the arc power (W), η is the arc efficiency, r_{eff} is the effective arc radius (m), U is the weld velocity (ms^{-1}), C_P is the specific heat of solid metal ($J\,kg^{-1}K^{-1}$), ρ is the density ($kg \cdot m^{-3}$), and T_L and T_a are the liquidus and ambient temperature (K), respectively. The numerator in Eq. (19) represents the effective energy absorbed by the work piece material per unit volume, while the denominator indicates the energy required to melt unit volume of work piece material from ambient temperature. The symbol N_{HI} embodies a combined influence of the welding process conditions and the material properties for the melting and the formation of weld pool. The computed value of N_{HI} for the present eight data sets are in the range of 1.11 to 2.15 as shown in Table 4. For a given material, high value of weld pool dimensions are linked to high values of N_{HI}. The use of a single optimum set of η, r^*, k^*, and μ^* to predict all the weld pool dimensions with reasonable accuracy corresponding to different welding conditions over this wide range of N_{HI} show the effectiveness of the integrated optimization and phenomenological heat transfer and fluid flow modeling.

After the uncertain parameters are optimized by GA, the integrated GA and the heat transfer and fluid flow model is next utilized to compute the alternative set of welding variables to attain a target weld geometry. Furthermore, the computed welding variable sets are then tested by conducting further experiments to examine the effectiveness of the procedure. The weld dimensions corresponding to the data set # 4 (Table 1) is chosen as the target geometry. The current, voltage, and weld velocity are considered as the main welding variables, and the goal is to determine multiple combinations of these three parameters, all of which can lead to the target weld geometry. To start the selection of multiple combinations of welding variables, it is first necessary to set a realistic range for each. This range is decided based on the experiences gathered during in-house experimental work, and the results reported in the literature [31, 32]. The feasible ranges of welding current, voltage, and velocity are considered as 100–200 A, 9–15 V, and 4–10 mm/s, respectively.

Figure 10 shows the randomly generated and diversely distributed initial population containing one hundred individuals each of which contains a set of values for the current, voltage, and velocity within their respective specified ranges in the nondimensional form. The minimum current (I_{mn} = 100 A), the minimum voltage (V_{mn} =

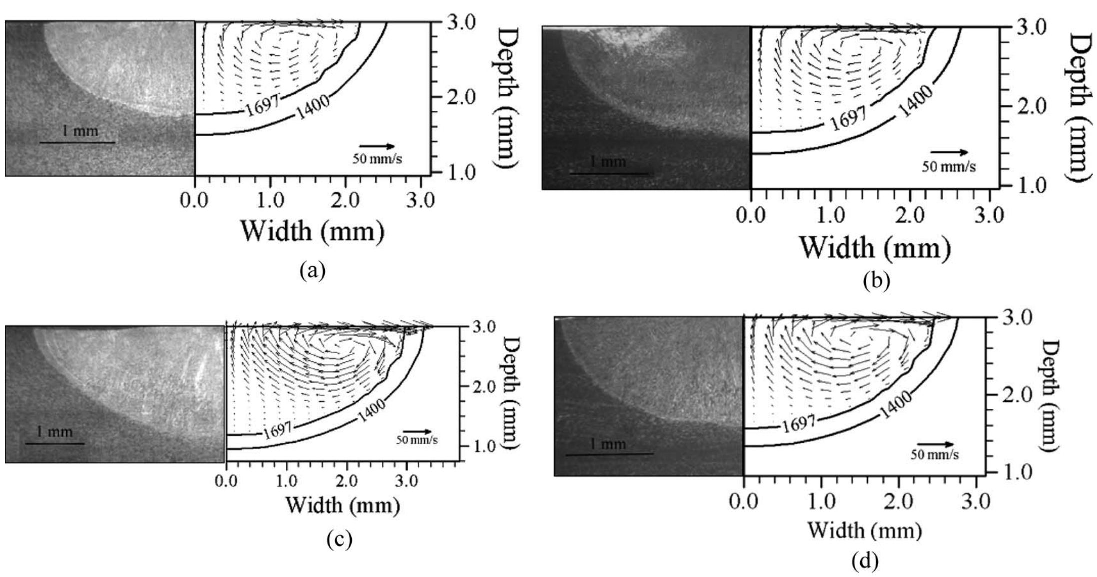

FIGURE 9.—Comparison of measured weld macrographs and the corresponding computed weld pool profiles for (a) data set index 1; (b) data set index 2; (c) data set index 6; and (d) data set index 7 in Table 1. The computations are performed using optimum values of uncertain parameters presented in Table 3.

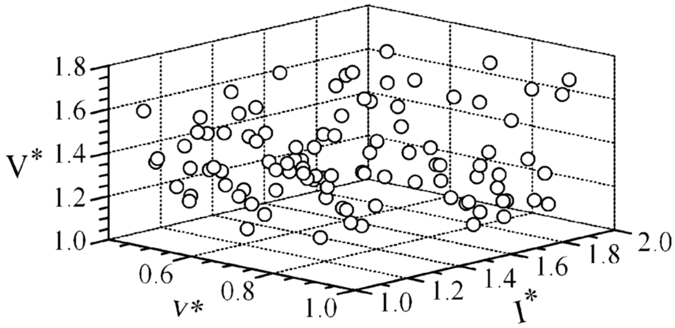

FIGURE 10.—Distribution of initially generated random populations each of which consists of a value of weld current, voltage, and weld velocity for estimation of multiple sets of welding variables to achieve a target weld geometry indicated in data set # 4 in Table 1.

9 V), and the maximum weld velocity ($v_{mx} = 10$ mm/s) in their respective specified ranges are considered as references for nondimensionalization of the corresponding variables. Figure 11(a) depicts the distribution of the objective function, $O(f)$, as a function of nondimensional welding current (I^*) and nondimensional weld velocity (v^*) corresponding to the initial population. It is noteworthy that computations of $O(f)$ now requires running of the convective heat transfer model for all the hundred individuals in the initial population and compare the computed weld dimensions with the measured values corresponding to the data set # 4 in Table 1. Thus, the parameter M in Eq. (15) equals to one and corresponds to the data set # 4. Small values of $O(f)$ in the range between 0.0 to 0.2 in Fig. 11(a) favor the existence of multiple combinations of process parameters that can possibly yield the target weld dimensions. Figure 11(b) depicts the distribution of $O(f)$ as a function of nondimensional welding current (I^*) and weld velocity (v^*) after tenth generations. About 10 sets of process parameter combinations achieved $O(f)$ even lower than 0.03. Figure 12 depicts eight optimized combinations of nondimensional welding current (I^*), voltage (V^*), and weld velocity (v^*) obtained after fifteenth generations. Each of these variable combinations had values of $O(f)$ smaller than 0.005. The actual values of $O(f)$ corresponding to each of these eight process parameter combinations are presented in Table 5. The minimum value of $O(f)$ after fifteen generation is 1.0×10^{-4} and corresponds to welding current, voltage, and weld velocity of 106.1 A, 12.5 V, and 4.8 mm/s, respectively. The eight possible solution sets are distributed throughout the entire solution space (Fig. 12) indicating the existence of multiple paths to attain the same weld geometry. The diversity of the multiple solution sets is also observed in Table 5 that cover the welding current ranging from 106 to 167 A, voltage from 9.8 to 14.4 V, and weld velocity from 4.3 to 9.6 mm/s. The weld pool dimensions corresponding to each individual solution sets are shown in Table 5. The computed values of nondimensional heat index (N_{HI}) had values between 1.1 to 1.4 for the eight solutions given in Table 5. The value of N_{HI} is 1.1 corresponding to the actual experimental condition (data set # 4 in Table 1) of the target weld geometry. Since the calculation procedure of N_{HI} is independent of weld pool dimensions, the small range of values of N_{HI} for all the eight solutions indicates a common feature among the diverse solutions.

Figure 13(a) shows the target weld geometry for which the welding conditions and the weld dimensions are shown in data set index 4 of Table 1. Figures 13(b)–(i) refer to the weld geometries obtained by conducting experiments using welding conditions calculated by GA and presented in Table 5 as solution sets 1 to 8, respectively. Table 5

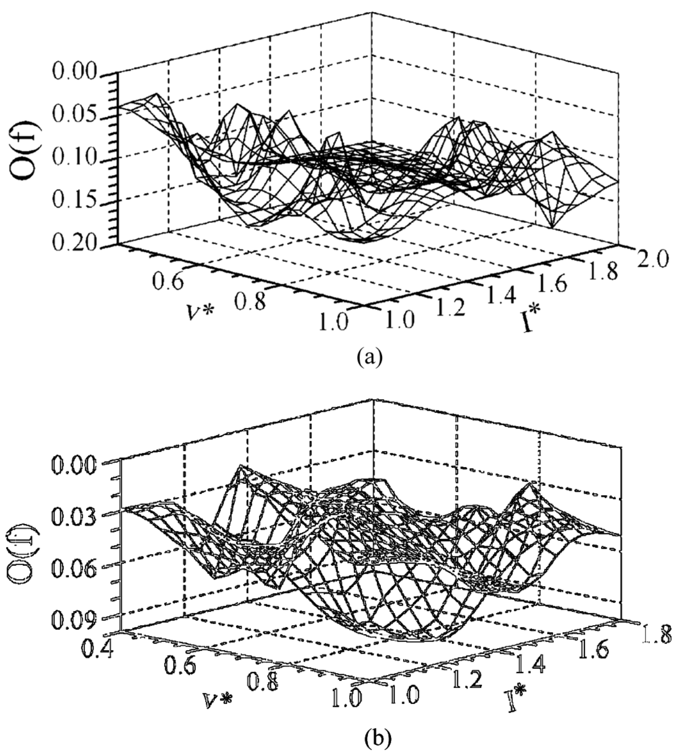

FIGURE 11.—(a) Distribution of $O(f)$ as a function of weld current and weld velocity corresponding to initial population described in Fig. 10; (b) distribution of $O(f)$ as a function of weld current and weld velocity after tenth generation.

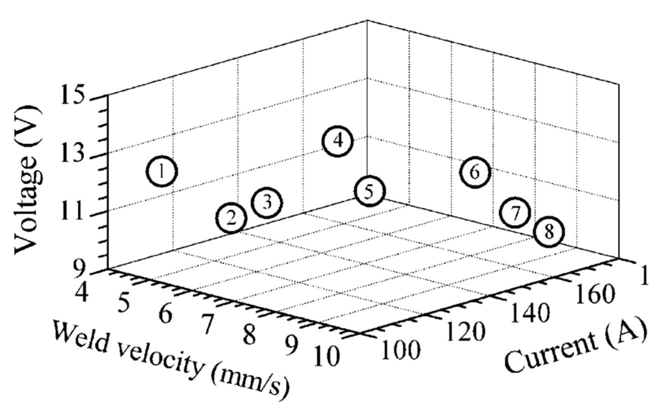

FIGURE 12.—Distribution of the finally selected eight multiple solutions sets to achieve the target weld geometry indicated in data set # 4 in Table 1.

TABLE 5.—Current, voltage and welding velocity combinations computed using GA. The calculated and the experimental values of weld dimensions are indicated by "cal" and the "exp," respectively.

Individual solution set	Current (A)	Voltage (V)	Velocity (mm/s)	$O(f)$	Width (mm) cal	Width (mm) exp	Penetration (mm) cal	Penetration (mm) exp	N_{HI}
1	133.98	9.77	4.31	0.0004	4.54	4.81	1.24	1.20	1.41
2	140.35	11.54	7.13	0.0007	4.57	4.89	1.24	1.21	1.13
3	134.77	10.56	5.10	0.0015	4.60	4.78	1.25	1.27	1.39
4	163.03	10.33	9.65	0.0049	4.34	4.60	1.18	1.22	1.07
5	116.96	14.38	8.16	0.0003	4.53	4.23	1.23	1.19	1.13
6	149.05	12.58	8.98	0.0037	4.63	4.90	1.28	1.30	1.14
7	106.09	12.47	4.82	0.0001	4.45	4.26	1.23	1.21	1.37
8	166.54	10.48	8.57	0.0005	4.55	4.65	1.24	1.25	1.11

also lists the dimensions of the welds measured in each case. The optimized welding variables in solution # 2 in Table 5 is almost the same as the welding variables in data set # 4 in Table 1, indicating effectiveness of the inverse modeling. Furthermore, the depth of penetration and width of all the welds presented in Fig. 13 and Table 5 do not differ more than 5% from the corresponding target weld dimensions. This similarity in geometry is counterintuitive because the welding variables were very different for the different solutions. For example, the current varied between 106 to 167 A, voltage varied from 9.8 to 14.4 V, and welding speed ranged from 4.3 to 9.6 mm/s in the solutions as shown in Table 5. The good agreement between the computed and the corresponding measured weld macrographs demonstrate the effectiveness of the GA-assisted convective weld pool model to find multiple welding variable sets to attain a target weld geometry by inverse modeling. In particular, the approach presented here also shows a promise that complex weld pool models can find greater use in actual industrial design because they can be restructured to improve their reliability and practical utility using GA.

6. SUMMARY AND CONCLUSIONS

A three dimensional convective heat transfer model of GTA welding of 304 stainless steel is integrated with a PCX G3 GA-based optimization to improve reliability

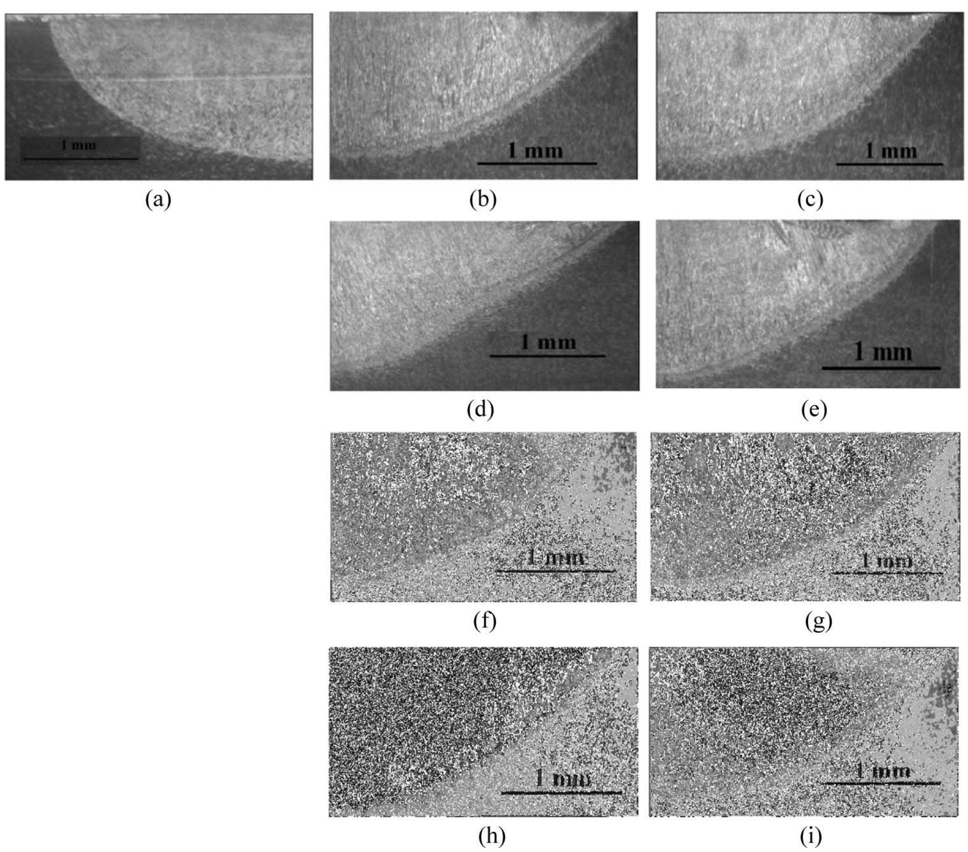

FIGURE 13.—(a) Weld macrograph for the target weld fabricated with parameters listed in Table 1, data set # 4; (b)–(i) refer to the weld geometries obtained by conducting experiments using welding conditions calculated by GA and presented in Table 5 as solution sets 1–8, respectively.

and practical utility of the calculations. The computational reliability was enhanced by GA-based optimization of arc efficiency, arc radius, effective thermal conductivity, and effective viscosity using a limited volume of experimental data which lead to superior performance of weld geometry computations under a wide variety of welding conditions. Secondly, the usefulness of the integrated model was demonstrated by the inverse modeling capability and demonstrating its effectiveness in tailoring weld geometry based on scientific principles. In particular, the capability of the inverse model to calculate multiple combinations of arc current, voltage, and welding speed to attain a target weld geometry was developed and rigorously tested. A weld geometry obtained from a welding experiment was selected as the target geometry. The inverse model was used to compute eight sets of welding variable combinations each of which is expected to lead to the target weld geometry. These eight welds were fabricated with the computed welding variable sets obtained from GA to test if the weld geometry in each case was similar to the target geometry. It was found that the welding variables computed by GA in one of the eight very closely matched the welding variables actually used to fabricate the target weld. In the remaining seven cases, the experimentally determined geometry agreed well with the target weld geometry. Several of these welding variable combinations were different from each other and were highly counterintuitive. The attainment of the target weld geometry via the GA-based search and the rigorous experimental verification of this capability indicate that it is possible to tailor weld attributes based on scientific principles using a combination of GA and a heat transfer and fluid flow model.

Appendix A: PCX G3 real number GA

In order to explain the principle of PCX-operated G3 model in GA [18, 19], an example is considered depicting the generation of two new individuals (offspring) out of three individuals (parents) from an *initial population*. First, three parents are selected from the *initial population* such that one of them corresponds to the lowest value of objective function. The other two are selected randomly. Considering the three parents as $\mathbf{P}_i = \{f_i^1 \quad f_i^2 \quad f_i^3 \quad f_i^4\}$ (where $i = 1, 3$), the arithmetic mean vector of them is calculated as $\mathbf{g} = \frac{1}{3}\sum_{i=1}^{3}\mathbf{P}_i$. Selecting one parent (say, p) at random, a direction vector, $\mathbf{d}_p$, and the mean of the perpendicular distances between the direction vector and each of the other two parents, $\overline{D}_p$, are calculated as

$$\mathbf{d}_p = \mathbf{P}_p - \mathbf{g},$$
$$\overline{D}_p = \frac{1}{2}\sum_{i=1, i\neq p}^{3}\left\{\left|\mathbf{P}_i - \mathbf{P}_p\right|^2 - \left(\frac{(\mathbf{P}_i - \mathbf{P}_p)\cdot \mathbf{d}_p}{\left|\mathbf{d}_p\right|}\right)^2\right\}^{\frac{1}{2}}. \tag{A.1}$$

An offspring, $\mathbf{y}_p$, is next created as

$$\mathbf{y}_p = \mathbf{P}_p + \omega_\zeta \mathbf{d}_p + \omega_\eta \overline{D}_p \mathbf{E}_p, \tag{A.2}$$

where $\mathbf{y}_p = \{f_p^1 \quad f_p^2 \quad f_p^3 \quad f_p^4\}$ and $p = 1, 2$ corresponds to the two new individuals in terms of their vector components. The second and third terms in RHS of Eq. (A.2) depict the improvement in the off-spring over successive generations. The improvement is always directed towards the best fitness value, i.e., the minimum value of $O(f)$. The term $\mathbf{E}_p$ is calculated as

$$\mathbf{E}_p = \hat{u} - \left(\frac{(\mathbf{d}_p)}{\left|\mathbf{d}_p\right|}\cdot\frac{(\mathbf{d}_p)}{\left|\mathbf{d}_p\right|}\right)\hat{u} \tag{A.3}$$

and is referred to the orthonormal base that spans the subspaces perpendicular to $\mathbf{d}_p$. In Eq. (A.3), $\hat{u}$ is the unit vector along the orthonormal direction. The parameters ω_ς and ω_η are zero-mean normally distributed variables with standard deviations of σ_ς and σ_η, respectively. Figure 14 describes the overall solution scheme that embeds the numerical heat transfer model within the GA-based optimization module. The PCX-operated G3 model is used twice in the overall solution procedure as indicated in Fig. 14.

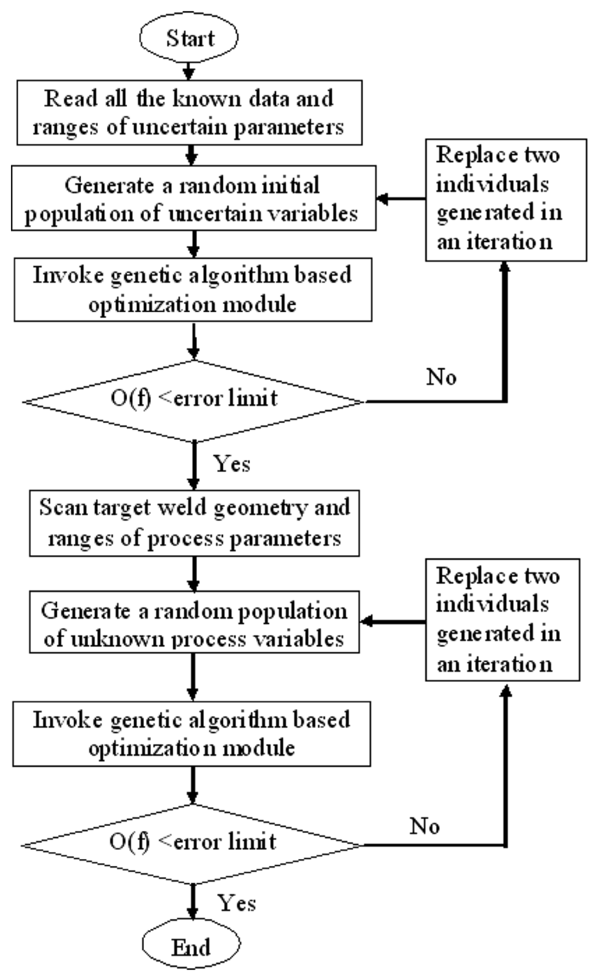

Figure 14.—Flow-chart of PCX G3 GA optimization algorithm.

Appendix B: electromagnetic force field

The Laplace equation for the distribution of electrical potential in cylindrical co-ordinate system is given by

$$\frac{\partial^2\Phi}{\partial r^2}+\frac{\partial\Phi}{r\partial r}+\frac{\partial^2\Phi}{\partial z^2}=0. \tag{B.1}$$

The boundary conditions for the potential field inside the workpiece are:

$$\text{Radial Boundary: } \Phi(h,z)=0 \tag{B.2}$$

$$\text{Bottom: } \frac{\partial\Phi(r,c)}{\partial z}=0 \tag{B.3}$$

$$\text{Top: } \frac{\partial\Phi(r,0)}{\partial z}=f(r)=-\frac{Id_I}{\pi r_b^2}\exp\left(-\frac{r^2 d_I}{r_b^2}\right), \tag{B.4}$$

where h is the maximum radius, z is the vertical distance from the origin located at the top surface, c is the thickness of the workpiece, I is the arc current, r_b is the arc radius, and d_I is the arc current distribution factor. The solution for Eq. (B.1) can be written in the form of a Fourier integral as

$$\Phi(r,z)=\frac{I}{2\pi\sigma_e}\int_0^\infty \exp\left(-\frac{\lambda^2 r_b^2}{4d_I}\right)\times J_0(r\lambda)\frac{\cosh[\lambda(c-z)]}{\sinh(\lambda c)}d\lambda, \tag{B.5}$$

where σ_e is electrical conductivity, and J_0 is the Bessel function of zero order and first kind. Considering the axi-symmetric condition, the magnetic field components in radial (i.e., B_r), and vertical directions (i.e., B_z) are assumed to be zero. Thus, from Ampere's law,

$$B_\theta=\frac{\mu_m}{r}\int_0^r rJ_z dr, \tag{B.6}$$

where B_θ is the angular component of the magnetic field, and μ_m is the magnetic permeability (1.26×10^{-6} H/m). The radial (J_r) and axial (J_z) components of the current density vectors can now be obtained from Ohm's law:

$$J_z=\frac{I}{2\pi}\int_0^\infty \lambda J_o(\lambda r)\exp\left(-\lambda^2 r_b^2/4d_I\right)\frac{\sinh[\lambda(c-z)]}{\sinh(\lambda c)}d\lambda \tag{B.7}$$

$$J_r=\frac{I}{2\pi}\int_0^\infty \lambda J_1(\lambda r)\exp\left(-\lambda^2 r_b^2/4d_I\right)\frac{\cosh[\lambda(c-z)]}{\sinh(\lambda c)}d\lambda, \tag{B.8}$$

where J_1 is Bessel function of first order and the first kind. Substituting Eq. (B.7) into Eq. (B.6), we get

$$B_\theta=\frac{\mu_m I}{2\pi}\int_0^\infty J_1(\lambda r)\exp\left(-\lambda^2 r_b^2/4d_I\right)\times\frac{\sinh[\lambda(c-z)]}{\sinh(\lambda c)}d\lambda. \tag{B.9}$$

The current density, **J**, and magnetic flux, **B**, calculated above in cylindrical coordinates can be transformed to the Cartesian coordinates using the following expressions:

$$J_x=J_r\frac{x}{\sqrt{x^2+y^2}} \tag{B.10a}$$

$$J_y=J_r\frac{y}{\sqrt{x^2+y^2}} \tag{B.10b}$$

$$B_x=B_\theta\frac{y}{\sqrt{x^2+y^2}} \tag{B.10c}$$

$$B_y=-B_\theta\frac{x}{\sqrt{x^2+y^2}} \tag{B.10d}$$

$$B_z=0.0. \tag{B.10e}$$

The final expressions for the three components of the electromagnetic force are given by

$$F_x=J_y\cdot B_z-J_z\cdot B_y \tag{B.11a}$$

$$F_y=J_z\cdot B_x-J_x\cdot B_z \tag{B.11b}$$

$$F_z=J_x\cdot B_y-J_y\cdot B_x. \tag{B.11c}$$

Acknowledgments

Two of the authors gratefully acknowledge the financial support being provided by the Department of Science and Technology, Government of INDIA (Grant no. SR/S3/MERC-043/2004).

References

1. Kou, S.; Sun, D.K. Fluid flow and weld penetration in stationary arc welds. Metallurgical and Materials Transactions A **1985**, *16A*, 203–213.
2. David, S.A.; DebRoy, T. Current issues and problems in welding science. Science **1992**, *257*, 497–502.
3. Nandan, R.; DebRoy, T.; Bhadeshia, H.K.D.H. Recent advances in friction-stir welding—Process, weldment structure and properties. Progress in Material Science **2008**, *53* (6), 980–1023.
4. Oreper, G.M.; Eagar, T.W.; Szekely, J. Convection in arc weld pools. Welding Journal **1983**, *62* (11), 307s–312s.
5. Zhang, W.; Elmer, J.W.; DebRoy, T. Modeling and real time mapping of phases during GTA welding of 1005 Steel. Material Science and Engineering A **2002**, *A333*, 320–335.
6. Yang, Z.; Elmer, J.W.; Wong, J.; DebRoy, T. Evaluation of titanium arc weldment macro and microstructures modeling and real time mapping of phases. Welding Journal **2000**, *79* (4), 97s–112s.
7. Mishra, S.; DebRoy, T. Measurements and Monte Carlo simulation of grain growth in the heat-affected zone of Ti-6Al-4V welds. Acta Materilia **2004**, *52* (5), 1183–1192.
8. Mundra, K.; DebRoy, T. Calculation of weld metal composition change in high-power conduction mode carbon dioxide laser-welded stainless steels. Metallurgical and Materials Transactions B **1993**, *24B*, 145–155.
9. He, X.; DebRoy, T.; Fuerschbach, P.W. Probing temperature during laser spot welding from vapor composition and modeling. Journal of Applied Physics **2003**, *94* (10), 6949–6958.

10. Miller, R.; DebRoy, T. Energy absorption by metal vapor dominated plasma during carbon dioxide laser welding of steels. Journal of Applied Physics **1990** *68* (5), 2045–2050.
11. Hong, K.; Weckman, D.C.; Strong, A.B.; Zheng, W. Modelling turbulent thermofluid flow in stationary gas tungsten arc weld pools. Science and Technology of Welding and Joining **2002**, *7* (3), 125–136.
12. De, A.; DebRoy, T. Probing unknown welding parameters from convective heat transfer calculation and multivariate optimization. Journal of Physics D: Applied Physics **2004**, *37* (1), 140–150.
13. De, A.; DebRoy, T. A smart model to determine effective thermal conductivity and viscosity in the weld pool. Journal of Applied Physics **2004**, *95* (9), 5230–5240.
14. De, A.; DebRoy, T. Reliable calculations of heat and fluid flow during conduction mode laser welding through optimization of uncertain parameters. Welding Journal **2005**, *84* (7), 101s–112s.
15. De, A.; DebRoy, T. Improving reliability of heat and fluid flow calculations during conduction model laser spot welding by multivariable optimization. Science and Technology of Welding and Joining **2006**, *11* (2), 143–153.
16. Trivedi, A.; Suman, A.; De, A. Integrating finite element based heat transfer analysis with multivariate optimization for efficient weld pool modeling. ISIJ International **2006**, *46* (2), 267–275.
17. Goldberg, D.E. *Optimization and Machine Learning*; Pearson: New Delhi, India, 2006.
18. Deb, K. *Multi-Objective Optimization Using Evolutionary Algorithm*; Wiley: New York, 2001.
19. Deb, K.; Anand, A.; Joshi, D. A computationally efficient evolutionary algorithm for real-parameter optimization. Evolutionary Computation **2002**, *10*, 371–395.
20. Chakraborti, N. Genetic algorithms in materials design and processing. International Materials Review **2004**, *49* (3–4), 246–260.
21. Nandan, R.; Rai, R.; Jayakanth, R.; Moitra, S.; Chakraborti, N.; Mukhopadhyay, A. Regulating crown and flatness during hot rolling: A multiobjective optimization study using genetic algorithms. Materials and Manufacturing Process **2005**, *20* (3), 459–478.
22. Chakraborti, N.; Deb, K.; Jha, A. Genetic algorithm based heat transfer analysis of a bloom re-heating furnace. Steel Research **2000**, *71* (10), 396–402.
23. Winter, G.; Abderraman, J.C.; Jimenez, J.A.; Gonzalez, B.; Benitez, E.; Cuesta, P. Meshless numerical simulation of (full) potential flows in a nozzle by genetic algorithms. International Journal for Numerical Methods in Engineering **2003**, *43* (10–11), 1167–1176.
24. Hilbert, R.; Janiga, G.; Baron, R.; Thevenin, D. Multi-objective shape optimization of a heat exchanger using parallel genetic algorithms. International Journal of Heat and Mass Transfer **2006**, *49* (15–16), 2567–2577.
25. Nandan, R.; Lienert, T.J.; DebRoy, T. Toward reliable calculations of heat and plastic flow during friction stir welding of Ti-6Al-4V alloy. International Journal of Materials Research **2008**, *99* (4), 434–444.
26. Patankar, S.V. *Numerical Heat Transfer and Fluid Flow*; Hemisphere Publishing Corporation: New York, 1982.
27. Voller, V.R.; Prakash, C. A fixed grid numerical modeling methodology for convection-diffusion mushy region phase-change problems. International Journal of Heat and Mass Transfer **1987**, *30* (8), 1709–1719.
28. Brent, A.D.; Voller, V.R.; Reid, K.J. Enthalpy–porosity technique for modeling convection-diffusion phase change: application to the melting of a pure metal. Numerical Heat Transfer **1988**, *13*, 297–318.
29. Kumar, A.; DebRoy, T. Calculation of three-dimensional electromagnetic force field during arc welding. Journal of Applied Physics **2003**, *94* (2), 1267–1277.
30. DebRoy, T.; Majumdar, A.K. Predicting fluid flow in gas stirred systems. Journal of Metals **1981**, *33* (11), 42–47.
31. Mishra, S.; Debroy, T. A heat-transfer and fluid-flow-based model to obtain a specific geometry using various combinations of welding variables. Journal of Applied Physics **2005**, *98* (4), article number 044902, 1–9.
32. Mishra, S.; Debroy, T. A computational procedure for finding multiple solutions of convective heat transfer equation. Journal of Physics D: Applied Physics **2005**, *38* (16), 2977–2985.
33. Bag, S.; De, A. Development of a three-dimensional heat-transfer model for the gas tungsten arc welding process using the finite element method coupled with a genetic algorithm–based identification of uncertain input parameters. Metallurgical and Materials Transactions A **2008**, *39A* (11), 2698–2710.
34. Goodarzi, M.; Choo, R.; Touguri, J.M. The effect of the cathode tip angle on the GTAW arc and weld pool: I. Mathematical weld of the arc. Journal of Physics D: Applied Physics **1997**, *30* (19), 2744–2756.
35. He, X.; Fuerschbach, P.W.; DebRoy, T. Heat transfer and fluid flow during laser spot welding of 304 stainless steel. Journal of Physics D: Applied Physics **2003**, *36* (12), 1388–1398.
36. He, X.; Elmer, J.W.; DebRoy, T. Heat transfer and fluid flow in laser microwelding. Journal of Applied Physics **2005**, *97* (8), 084909.